

Modelling of material removal due to sliding wear caused by bulk material

Yan, Yunpeng; Helmons, Rudy; Carr, Michael; Wheeler, Craig; Schott, Dingena

DOI

[10.1016/j.powtec.2022.118109](https://doi.org/10.1016/j.powtec.2022.118109)

Publication date

2023

Document Version

Final published version

Published in

Powder Technology

Citation (APA)

Yan, Y., Helmons, R., Carr, M., Wheeler, C., & Schott, D. (2023). Modelling of material removal due to sliding wear caused by bulk material. *Powder Technology*, 415, Article 118109. <https://doi.org/10.1016/j.powtec.2022.118109>

Important note

To cite this publication, please use the final published version (if applicable). Please check the document version above.

Copyright

Other than for strictly personal use, it is not permitted to download, forward or distribute the text or part of it, without the consent of the author(s) and/or copyright holder(s), unless the work is under an open content license such as Creative Commons.

Takedown policy

Please contact us and provide details if you believe this document breaches copyrights. We will remove access to the work immediately and investigate your claim.



Modelling of material removal due to sliding wear caused by bulk material

Yunpeng Yan ^{a,*}, Rudy Helmons ^{a,b}, Michael Carr ^c, Craig Wheeler ^c, Dingena Schott ^a

^a Department of Maritime and Transport Technology, Delft University of Technology, 2628 CD Delft, the Netherlands

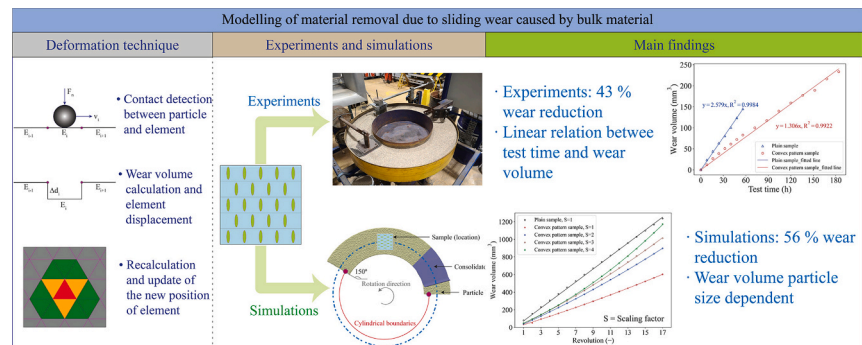
^b Department of Mineral Processing and HSE, Norwegian University of Science and Technology, 7031 Trondheim, Norway

^c School of Engineering, The University of Newcastle, Callaghan 2308, Australia

HIGHLIGHTS

- The convex pattern sample reduces sliding wear by 43% compared to a plain sample.
- The convex pattern sample reduces wear by altering the flow behaviour of bulk material.
- The deformation due to wear of the convex pattern weakens the effectiveness of wear reduction.
- The wear volume of the convex pattern sample has a quadratic relation with the revolutions.

GRAPHICAL ABSTRACT



ARTICLE INFO

Keywords:

Convex pattern surface
Wear deformation
Wear experiment
Particle size
Scaling factor

ABSTRACT

A convex pattern surface has been proposed and optimized to reduce sliding wear of bulk handling equipment by adjusting the flow behaviour of bulk material. This study aims at modelling the surface deformation of the convex pattern sample to investigate how effectively the sample reduces sliding wear. Archard wear model and a deformable geometry technique are combined to capture the sample deformation. A short-time laboratory wear experiment is performed as a benchmark to validate the numerical model. The simulation results indicate that there is a linear relation between the wear volume of a plain sample and the simulated revolutions, while the convex pattern sample has a quadratic trend. The wear distribution displays that the convex pattern accounts for the majority of wear of the sample. The contact behaviour demonstrates that the convex pattern facilitates the rolling of particles, resulting in the reduction of sliding distance. The numerical results indicate that the deformed convex pattern sample leads to lower overall sliding wear than a plain sample, although its effectiveness weakens as wear evolves.

1. Introduction

Bulk solids handling plays a significant role in a range of industries, such as the mining, agricultural, chemical, and pharmaceutical

industries [1]. In the mining industry, the process of transferring bulk solids such as iron ore leads to surface wear of handling equipment. Studies show that approximately 82% of the energy loss is attributed to the bulk material sliding along the bottom of the chute, while 9% of the

* Corresponding author.

E-mail address: Y.Yan@tudelft.nl (Y. Yan).

<https://doi.org/10.1016/j.powtec.2022.118109>

Received 26 July 2022; Received in revised form 14 November 2022; Accepted 16 November 2022

Available online 23 November 2022

0032-5910/© 2022 The Author(s). Published by Elsevier B.V. This is an open access article under the CC BY license (<http://creativecommons.org/licenses/by/4.0/>).

loss is due to the material sliding against the side walls [2]. Sliding wear can be characterized as a relative motion between two solid surfaces in contact under load [3], and long-term wear leads to surface deformation and accelerates damage to the equipment, reducing its lifespan.

To reduce wear both at micro [4,5] and macro [6] scales, a surface equipped with configurations (e.g. circular, triangular, and elliptical) are applied to the multiple fields mentioned above. For the elliptical texture, it has been used to reduce wear of ploughs [7], drills [8], lubricated contacts [9], and so on. Similarly, to reduce the sliding wear of bulk solids handling equipment, a convex pattern surface inspired by a bionic design method [10] is proposed [11] and optimized [12] by using the discrete element method (DEM) [13].

In the context of wear evaluation, DEM is a useful approach to predicting equipment wear caused by bulk material. On the one hand, DEM models wear without considering geometrical deformation. This method is widely used to investigate the linear wear and distribution of a ball mill [14–16], tumbling mill [17–19], mining hoppers [20], agricultural tines [21], and soil raper tin [22]. On the other hand, researchers are interested in surface deformation caused by the contact with bulk material. However, the relevant studies are limited when referring to both the surface deformation and contact with bulk material at the same time numerically and experimentally. Kalala et.al [23] first applied DEM to estimate adhesion, abrasion, and impact wear in dry ball mills, using industrial wear measurements for further validation. Then, Boemer et.al [25] proposed a generic wear prediction procedure based on DEM for ball mill liners in the cement industry. By obtaining a global wear constant and analyzing the mesh size sensitivity both in 1D and 2D, the predicted wear profile can be matched to measurements through a mesh smoothing technique. Next, Schramm et.al [26] modelled a scratch test to study abrasive material loss caused by soil tillage and compared it with a cross-section profile. Recently, Esteves et.al [24] compared the wear profile of the screw liner used in industrial vertical stirred mills to the measurements after >3000 h by using scaling-up procedures. The wear volumes obtained from the DEM model agree closely with the measured results at a specific velocity.

It must be noted, however, that these wear deformation studies are limited to smooth or regular geometrical shapes. For a non-smooth convex pattern surface used to reduce sliding wear, it is essential to model the deformation of this sample, as this may influence its ability to reduce sliding wear. To study the deformation caused by sliding wear, a pin-on-disc test was performed [27] as a benchmark and modelled [28] using DEM by implementing a geometrical deformation technique [29]. This test was used to verify the numerical results by comparing wear contour and wear volume with the test results, which implies that the geometrical deformation technique makes it possible model the wear deformation caused by a single contact. However, the deformation of the convex pattern sample due to wear is not revealed at the bulk level. Up to the best knowledge of the authors, this is the first work where the experiments and modelling are combined to demonstrate the surface deformation of a convex pattern configuration due to the contact with bulk material. By investigating the sample deformation, the effectiveness of the configuration on wear reduction can be better understood when surface deformation evolves. The aim of this study is to investigate to what extent the convex pattern sample continues to reduce sliding wear compared to a plain sample. The study consists of five steps. First, the geometrical deformation technique and Archard wear model are explained. Second, the wear experiment is performed in a circular wear tester. Third, a numerical DEM model is developed and the stability of the model is evaluated. Fourth, the numerical model is benchmarked with the result of the experiment, and the wear behaviour and contact behaviour with particles of the convex pattern sample are analyzed. Fifth, the main findings and conclusions are shared.

2. DEM with geometrical deformation technique

The discrete element method (DEM) was developed by Cundall and

Strack [13] to model particle systems by tracking the movement of each particle and its interaction with its surroundings over time. The motion of discrete spheres in DEM is governed by Newton's second law of motion. The Hertz–Mindlin no-slip contact model is a non-linear elastic contact model and is appropriate for non-cohesive granular materials [30]. This model consists of two springs, two dampers, and a slider as illustrated in Fig. 1. The springs are used to represent particle stiffness in normal and tangential directions. Two dampers are used to model the damping forces, and the slider is applied to generate a friction force.

The surface deformation is modelled by a geometrical deformation technique [29] in EDEM [31] combined with the Archard wear model [32] shown in Fig. 2. The highlighted part demonstrates the process of calculating wear volume and updating the mesh position of the geometry, as explained below.

The Archard wear model is integrated into this technique, as this model is widely used both for particles and geometries, e.g. for evaluating the wear of ballast and abrasive grain [33,34], for predicting the wear of mill lifters [35], and for predicting local failures caused by abrasive wear on tipper bodies [36]. This model has also been successfully applied to evaluate the wear behaviour of the convex pattern surface [12]. The Archard wear model is shown in Eq. (1).

$$V = k \frac{F_n l_s}{H_s} \quad (1)$$

where V (mm^3) is the wear volume, H_s (N/mm^2) is the hardness of the surface, k is a dimensionless wear coefficient, F_n (N) is the normal force applied to an equipment surface, and l_s (mm) is the sliding distance.

Eq. (1) can be expressed by a derivative formula denoted as Eq. (2),

$$dV = \frac{k F_n \|v_t\| dt}{H_s} = \alpha_s F_n \|v_t\| dt \quad (2)$$

where $\alpha_s = k/H_s$ represents the wear coefficient. dV , $\|v_t\|$, and dt denote the increment of wear volume of the material removed, relative tangential velocity, and time increment, respectively.

The detailed sequence of mesh deformation is illustrated in Fig. A.1.

3. Wear experiments

3.1. Experiment setup

A convex pattern surface, as shown in Fig. 3, is defined by five parameters [12]: major and minor radii a and b , vertical and horizontal distances c and d , and height h . To analyze the wear distribution, the sample is split into 5 columns (with Col_1 indicating column 1) along the bulk flow direction, and each convex element is labelled separately, moving from the inner side to the outer side of the sample. For example, the first convex element in the first column is labelled C11.

The convex pattern and plain samples are tested in an improved circular wear tester to make it possible to test a submerged sample in addition to the traditional face-down sample. The test rig is shown in

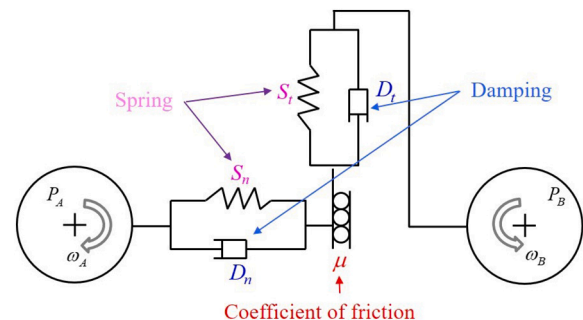


Fig. 1. Illustration of contact between two particles.

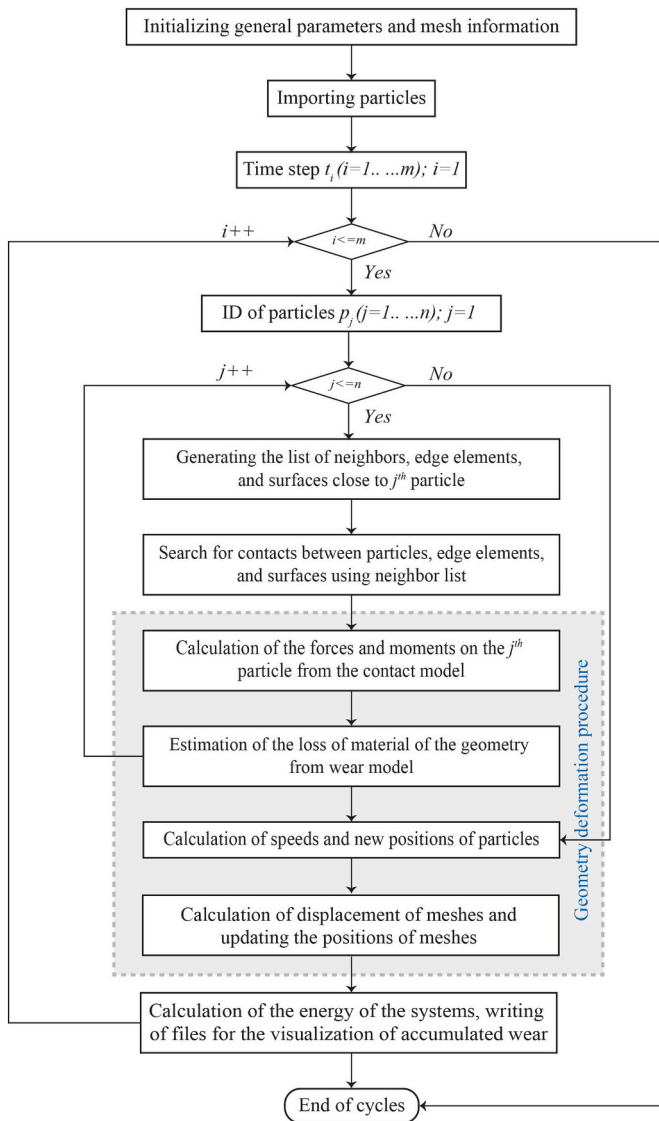


Fig. 2. Flowchart for calculating wear volume and updating deformation.

Fig. 4 and has the following features:

- 1) The outer and inner radii of the rotating annular bed are 500 mm and 290 mm, respectively.
- 2) By inclining the test specimen at a small angle in the bulk flow direction, evenly distributed wear over the entire surface of the test specimen can be obtained.
- 3) A test specimen holder for easy placement of a standard sample (Fig. 4 (b)).
- 4) A consolidator is used to level the surface of the wear media before they are presented to the test specimen.
- 5) Two wear samples (face-down and submerged), representing two wear scenarios, can be tested at the same time.

Table 1 lists the test parameters and sample properties. River gravel is used as a wear medium and this material is classified as dry, non-cohesive, and free-flowing, with the particle size distribution shown in Fig. 5. The test specimen is made from polyethylene (PE), which is designed to meet the full range of material flow, friction and wear challenges associated with bulk material. In addition, this material makes it possible to achieve sufficient material wear within a reasonable testing period. The specimen is mounted at a depth of 85 mm with an

incline angle of 2 degrees.

The tester has a rotational velocity of 1.52 rad/s. Based on the dimensions of the tester, the speed at the center of the sample is 0.6 m/s, resulting in test distance of 2.16 km per hour. The specimen is weighed by an electronic balance with 0.001 g precision and is scanned every 8 h by the Artec Space Spider 3D scanner with 0.05 mm accuracy. As the wear loss of the plain sample follows a linear relation with the test period [37], the plain sample is tested 56 h to cut experimental time. To ensure sufficient deformation on the convexes, the convex pattern sample is continued to be tested to 184 h.

3.2. Wear contour reconstruction

3.2.1. Experimental results

Continuing on from the previous study [12], this study focuses on the submerged sample illustrated in Fig. 4. Fig. 6 compares the wear volume loss of a plain and convex pattern sample. After 56 h of testing, the plain and the convex pattern sample generated 145.2 mm³ and 82.8 mm³ of volume loss, respectively. Compared to the plain sample, the convex pattern sample reduces wear by 43%. There is a linear correlation between wear volume and test time for both the plain sample and the convex pattern sample and the corresponding regression models have high coefficient of determination ($R^2 > 0.99$), as shown in Fig. 6. The wear volume is fitted with a linear equation, as wear volume increases by 17.9 ± 1.7 mm³ and 10.2 ± 1.2 mm³ at each time interval for the plain and convex pattern sample, respectively. Besides, operational conditions are kept consistent and the deformation of the sample has a minor effect on flow behaviour, so it is reasonable to assume that the wear rate is constant in this time period.

Furthermore, the wear contour was reconstructed to evaluate the deformation behaviour of the convex pattern (Please see the detailed procedure of wear contour reconstruction in Fig. A.2). Fig. 7 compares the extracted wear contours from the point clouds. The C11, C13, and C15 are taken as references and the reasons are explained in Section 5.2.2. The maximum deformations in vertical direction are 0.34 mm, 0.30 mm, and 0.35 mm for these three convexes, respectively. From the side view, it can be seen that the three convex elements deform in similar ways where the front part of the convex displays more obvious deformation than the back part as the front part initializes the contact with particles. From the front view, the deformations are manifested differently depending on the location of the convex element on the sample. For C11, the inner side deforms more heavily than the outer side, while C15, on the other hand, exhibits more severe deformation on the outer side. Overall, C11 and C15 indicate severer deformation than C13 as these convexes are located at the sides of the sample.

4. Numerical model

4.1. Numerical model setup

The DEM simulation setup is shown in Fig. 8. To cut computational costs, cylindrical boundaries with 150 degrees are used which allow particles flowing out from one side to re-enter from another side at the corresponding locations. The particle size is scaled up by 3, as the previous study shows that particle size has a minor effect on the sliding wear of the plain sample [38]. A consolidator similar to the one used in the experiment setup is applied to flatten the particle bed. The test sample is located at a depth of 90 mm in the particle bed at a 2-degree incline. The particle bed has a rotational rate of 90 deg./s, which means that a 150-degree revolution takes 1.67 s. For other parameters used in the numerical model, see the previous study [12].

4.2. Stability evaluation

The material flow in the numerical model should reach a stable state before the sample deformation is modelled. The stability of the system is

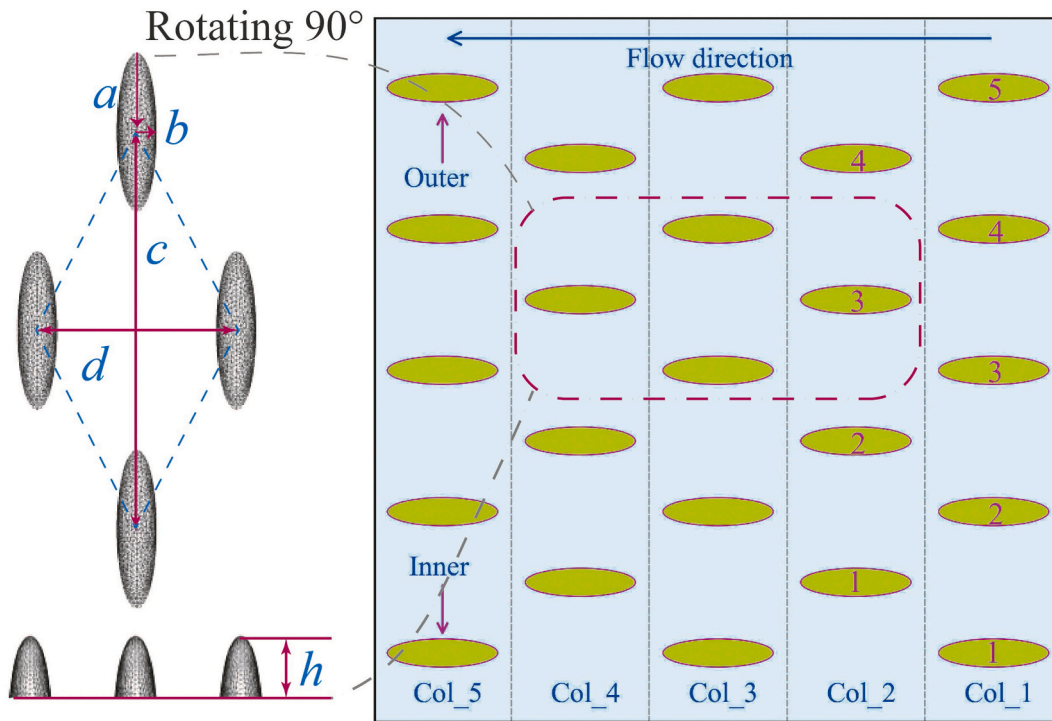


Fig. 3. Convex pattern sample (a = 8 mm, b = 2 mm, c = 20 mm, d = 40 mm, h = 6 mm).

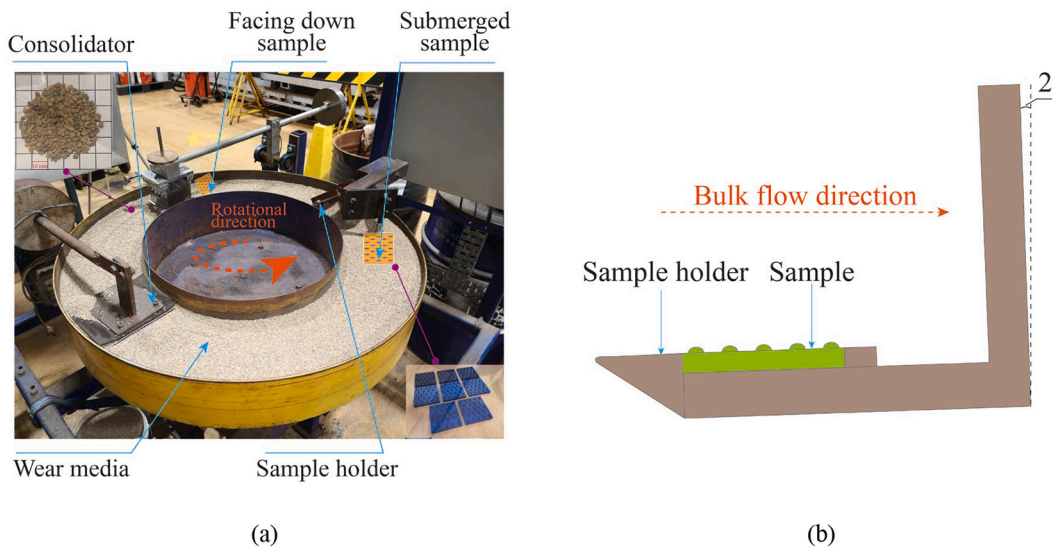


Fig. 4. Wear tester (a) Improved circular wear tester holding a traditional face-down sample and a submerged sample [37], (b) sample holder with inclined angle.

evaluated by three criteria, including particle velocity, particle bed height, and wear rate. The particle velocity and particle bed height demonstrate the particle flow behaviour and the wear rate indicates the wear behaviour of a sample. The coefficient of variation (CoV), as expressed by Eq. (3), is used to estimate the variability of the criteria.

$$C_v = \frac{\sigma}{\mu} \tag{3}$$

where C_v , σ , and μ are coefficient of variation, standard deviation of each revolution, and the mean value at each revolution, respectively.

Fig. 9 depicts the CoV of the three evaluation criteria. It should be noted that the particle flow behaviour is based on the particles over the sample. The coefficients of the three criteria drop after the first

revolution before stabilizing. For the particle flow behaviour, the particle bed height and particle velocity demonstrate a small fluctuation, which indicates that the particles flow smoothly after a transition period. For the wear rate, the convex pattern sample shows relatively high variation, which remains between 5.7% and 8.0% from revolution 6 onwards. Based on the evaluation of the coefficients, the numerical system reaches a stable state after 6 revolutions.

5. Numerical result analysis

5.1. Benchmark of numerical model

Based on previous study [28], the finer the mesh, the more precisely we can estimate surface deformation. However, if the convex pattern

Table 1
Summary of test parameters.

Categories	Parameters	Values
Wear medium	Bulk density (kg/m ³)	1455
	Particle size d ₅₀ (mm)	2.65
	Particle shape	Irregular
	Moisture content	0.6%
	Material type	SIMONA PE1000
Wear sample properties	Ductility	ductile
	Density (kg/m ³)	930
	Shore hardness (D scale)	62
	Submerged depth (mm)	85
	Normal pressure (kPa)	1.2
Operational conditions	Inclination angle (deg)	2
	Rotational velocity (rad/s)	1.52
	Test interval (h)	8

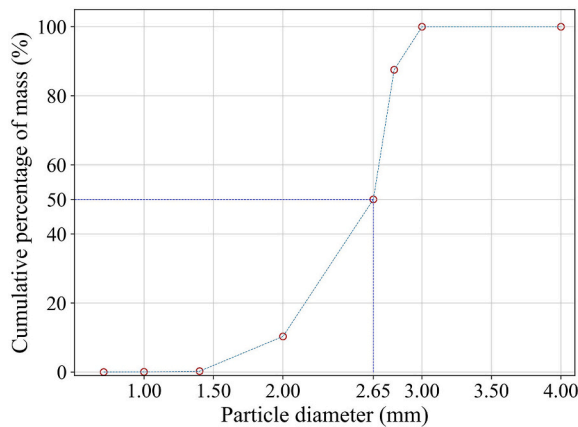


Fig. 5. Particle size distribution.

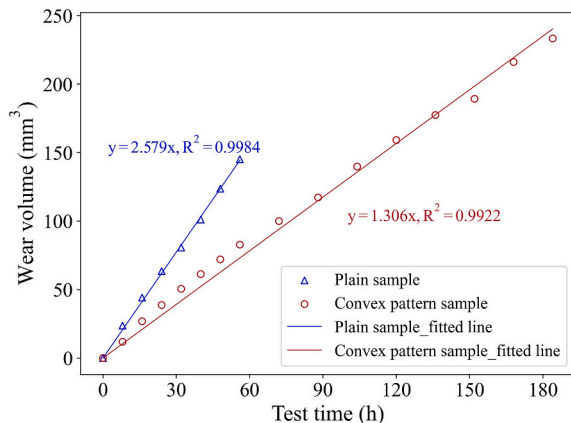


Fig. 6. Wear volume comparison from experiments.

sample is meshed with fine mesh (e.g., 0.1 mm), the total amount of elements exceeds 2.5 million, leading to unpractical computation times. To help cut computation time, the effect of mesh size on wear behaviour is investigated.

Fig. 10 compares the relative wear volumes of the samples with mesh size from 0.1 mm to 1 mm after two revolutions. The wear volume of the plain sample with mesh size of 0.1 mm is set as a reference value. The average relative wear volumes are $97.9\% \pm 1.8\%$ and $56.9\% \pm 2.8\%$ for the plain and convex pattern samples, respectively. Quantitatively, the mesh size has a negligible effect on wear volume.

For the wear contour, convex element C15 is selected, as shown in Fig. 3, since it suffers the most severe wear, as mentioned in Section

5.2.1. Fig. 11 shows the effect of mesh size on wear deformation of the convex element after two revolutions. As can be seen from the side view, the deformation is concentrated mainly around the front part of the convex, since this part is in direct contact with the bulk flow. The front view shows that the outer side of the convex element undergoes severe deformation. Combining the side and front views of the wear contours, it demonstrates that the surface undergoes similar deformations with different mesh sizes. As mesh size has a minor effect on wear in both quantitative and qualitative terms, it is set at 1 mm.

It is assumed that, after the material flow reaches a stable state, the total 56 h (8 intervals) of laboratory testing can be modelled in 2 revolutions by applying a scaling factor [28]. As a benchmark, the wear volume of a plain sample with particle scaling factor is set at 3 and compared with the wear volume of the test result. If the wear volume of the plain sample is comparable to that of the test result, the wear coefficient can be determined [28]. Fig. 12 compares the wear volume between the experimental and the numerical results for a wear coefficient of $5 \times 10^{-9} \text{ Pa}^{-1}$ in the numerical model. For the plain sample, the wear volumes of the test and the numerical model are 145.16 mm^3 and 154.06 mm^3 , respectively, with a difference of 5.8%. Because of this small difference, the wear coefficient is chosen for the following simulations.

Particles with scaling factor 1, 2, and 4 are investigated to test the validity of the numerical model. Fig. 12 shows that particle size has a minor effect on the wear volume of the plain sample, with a fluctuation of 14%, because of the wall effect that occurs when applying a coarse graining technique. The wear volume of the convex pattern sample is lower than that of the plain sample and it increases with particle size. The relation between particle size and wear volume of both the plain and convex pattern samples is consistent with the previous study [38].

For a particle scaling factor of 1, the convex pattern sample reduces wear volume by 68.9% and 43.0% in the simulation and the experiments, respectively. There are two reasons for this. First, the numerical model only applies a sliding wear model, while the experiment comprises multiple coexistent wear modes, such as wear caused by rolling particles. Second, the particles are irregular in the experiments, but they are simplified and spherical in simulations. The angular particles tend to accelerate surface deformation, as stress is concentrated at the corners of the particles.

A scaling factor is defined by the ratio of the total distance of the experiment to that of the simulation. Based on the operational testing conditions listed in Table 1, the total sliding distances of the experiment and the simulation are 84.6 km and 2.142 m, so the scaling factor is set at 40000.

5.2. Wear behaviour comparison

5.2.1. Wear volume

To demonstrate to what extent the deformed convex sample continues to reduce sliding wear compared to a plain sample, the deformation model does not terminate until it encounters a convergence problem due to a mesh distortion issue [25]. With the wear coefficient of $5 \times 10^{-9} \text{ Pa}^{-1}$, the model is valid for the first 17 revolutions, with the corresponding wear result being shown in Fig. 13. The wear volume of a plain sample with a particle scaling factor of 1 is set as a reference. Fig. 13 indicates that the wear volume of the plain sample is higher than that of the convex pattern sample and increases linearly, while the convex pattern sample has a quadratic trend. The corresponding fitted equations are listed under Eqs. (4)–(8). The equations indicate that the higher the particle scaling factor, the more obvious the quadratic trend becomes.

$$y_{P1} = 73.64x, R^2 = 0.9994 \quad (4)$$

$$y_{C1} = 0.31x^2 + 30.29x, R^2 = 0.9997 \quad (5)$$

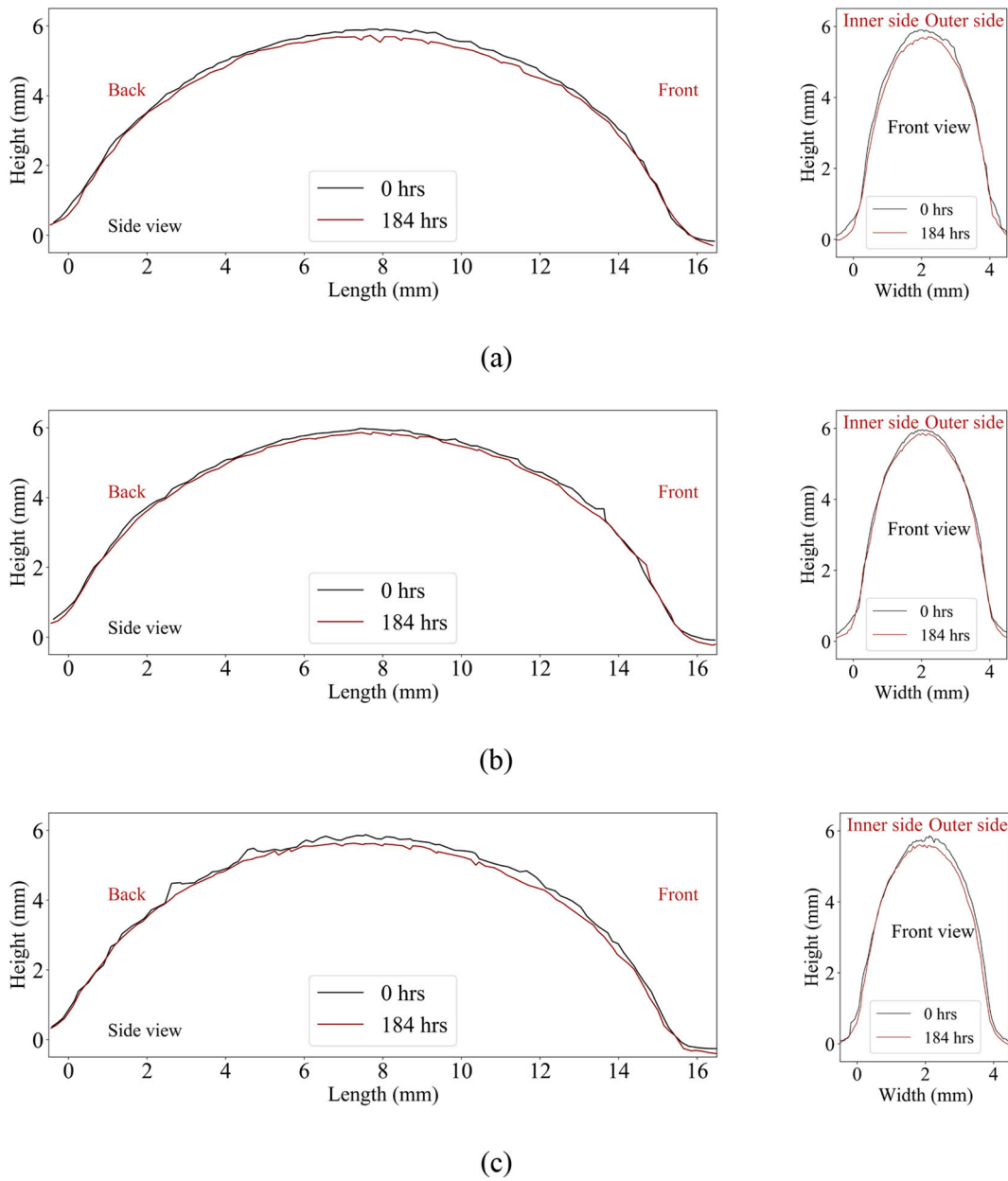


Fig. 7. Convex element deformation from experiments (a) C11, (b) C13, (c) C15.

$$y_{C2} = 0.59x^2 + 43.21x, R^2 = 0.99997 \quad (6)$$

$$y_{C3} = 0.78x^2 + 47.12x, R^2 = 0.99998 \quad (7)$$

$$y_{C4} = 1.57x^2 + 41.62x, R^2 = 0.99996 \quad (8)$$

where the subscripts P and C represent the plain and convex pattern sample, respectively. The number indicates the particle scaling factor.

As the experiment of 56 h is represented by 2 numerical revolutions, the 184 h are equal to 6.57 revolutions. Based on the Eq. (4) and (5), the wear volumes of the plain and convex pattern samples are 474.5 and 240.3 mm³, respectively, showing a 56% wear reduction. Similarly, the experimental result shown in Fig. 6 indicates 483.9 and 212.9 mm³ volume losses for the plain and convex pattern sample, leading to a 51% wear reduction. Quantitatively, the numerical model demonstrates 5% difference with the experimental results.

To better understand the relation between wear volume and number of revolutions, the average wear volume increment of individual ele-

ments shown in Fig. 14 is defined. It is denoted as the average wear volume increment of individual meshes between two revolutions. Eq. (9) is used to calculate wear volume increment.

$$\Delta v(j) = \frac{\sum_{i=1}^n [h(j+1)_i - h(j)_i] \cdot A_i}{n} \quad (9)$$

where j, n, and subscript i denote the number of revolutions, the number of elements, and the ith element, respectively. The $\Delta v(j)$, $h(j)_i$, and A_i represent the wear volume increment of jth revolution, wear depth of element i for j revolutions, and the area of mesh element, respectively.

For the plain sample, the wear volume increment decreases from 0.0022 mm³ to 0.002 mm³. For the convex pattern sample, it has an increasing trend for different particle scaling factors. The wear volume increases more slowly with a lower particle scaling factor than with a higher scaling factor. For a particle scaling factor of 4, the wear volume increment surpasses that of the plain sample at revolution 15, which means the wear volume of the sample increases faster than that of the

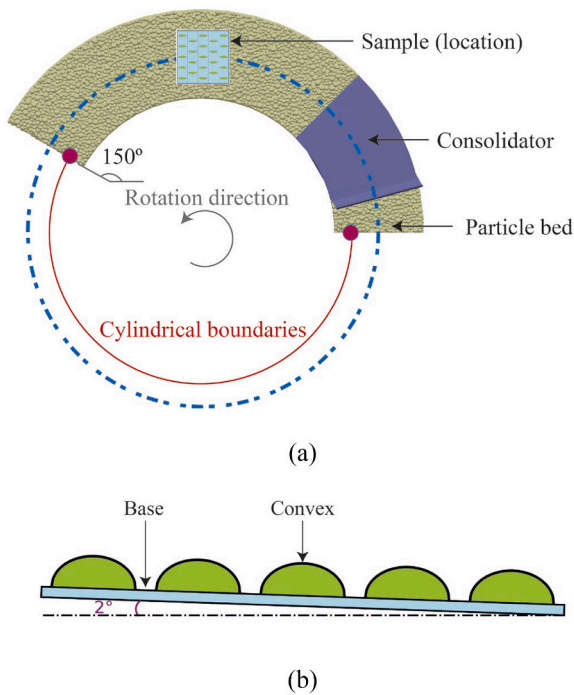


Fig. 8. Simulation setup. (a) particle bed settings, (b) inclination angle of sample.

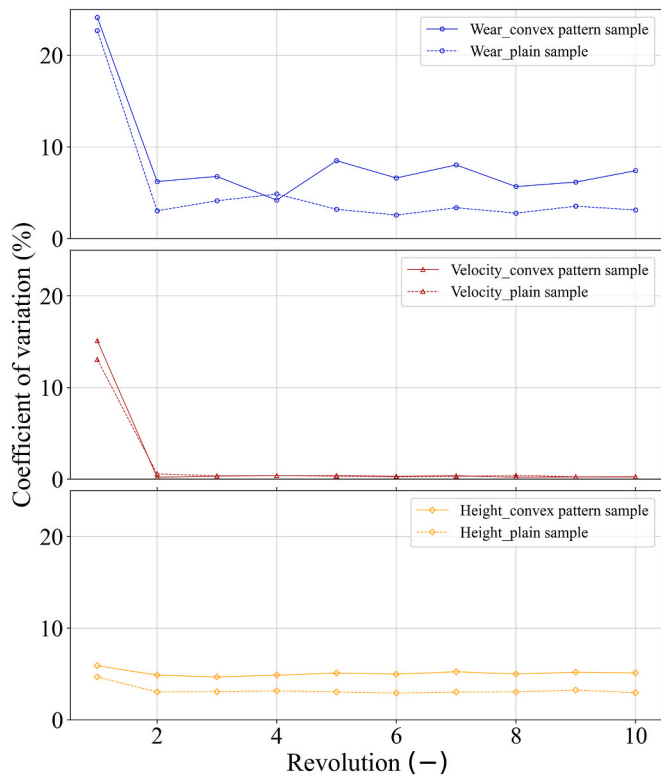


Fig. 9. Stability evaluation of the numerical model (Wear, velocity, and height represent sample wear rate, particle velocity, and particle bed height, respectively.)

plain sample. Moreover, it implies that the total wear volume of the sample can exceed the total wear volume of the plain sample after one specific revolution.

Fig. 15 depicts the wear volume of each column for both the convex

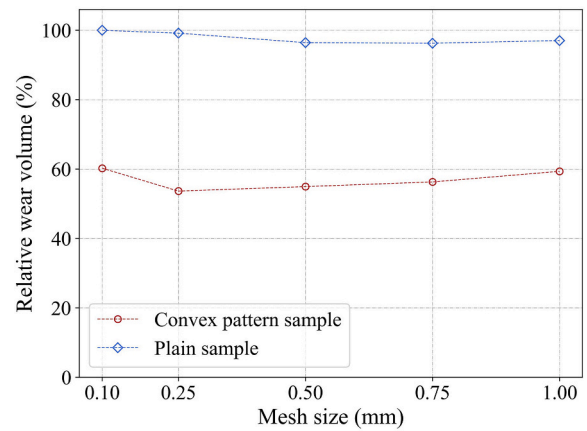


Fig. 10. Effect of mesh size on wear volume.

and plain samples. For the plain sample, the wear volume increases from column 1 to 5. For the convex pattern sample, the convex pattern accounts for 56% of the total wear volume of the sample. Column 1 shows the highest wear volume, as it guides and initializes the movement of particles when they come into contact with the sample. Besides, columns 1 and 5 see greater wear volume levels than columns 2 and 4, because the surface area of columns 2 and 4 is lower than the other 3 columns.

Fig. 16 compares the wear volume of individual convex elements as labelled in Fig. 3. Columns 1, 3, and 5 show a wide range of wear volumes from 7.6 to 31.6 mm³, while columns 2 and 4 show a relatively narrow range from 6.9 to 14.1 mm³. The convex elements located at the two sides of the sample demonstrate the maximum level of wear volume. This is because the convex elements located at the two outer ends of the sample have a weak effect on guiding and rolling particles. For a detailed explanation, see the previous study [12].

5.2.2. Wear distribution and reconstruction

Fig. 17 displays the wear distribution in two samples after 17 revolutions. For the plain sample shown in Fig. 17 (a), the wear is almost evenly distributed over the full sample. For the convex pattern sample shown in Fig. 17 (b), wear paths are formed among the convex elements because of the flow behaviour of particles. In addition, the majority of wear is transferred to the convex pattern, thus protecting the base.

Fig. 18 compares the deformation process of three convex elements in column 1, since this column suffers the most severe deformation, as shown in Fig. 15. C11 and C15 are located at the two ends of the sample and C13 is in the middle of column 1, as illustrated in Fig. 3. From the side view, these three convex elements follow a similar deformation trend. The front part of the convex elements suffers the most severe deformation, since this part comes into direct contact with particles. From the front view, it can be seen that the inner side of C11 and outer side of C15 show greater deformation. This implies that the convex pattern hardly affects the flow behaviour of particles at the two sides [12]. Furthermore, C15 is subject to the greatest degree of deformation because the particles at the outer end of a circular wear tester slide longer distances. Overall, the numerical model indicates a similar deformation trend with the experiment. As the effect of the coarse mesh on the reconstruction, the wear contour is rougher compared to that of the experiment.

5.3. Contact behaviour

5.3.1. Particle flow behaviour

Particle flow behaviour consists of the angular and transitional velocity of particles at the bottom layer, where the particles are directly affected by the convex pattern. Fig. 19 shows the angular velocity of particles. For the plain sample, the angular velocity stays within a

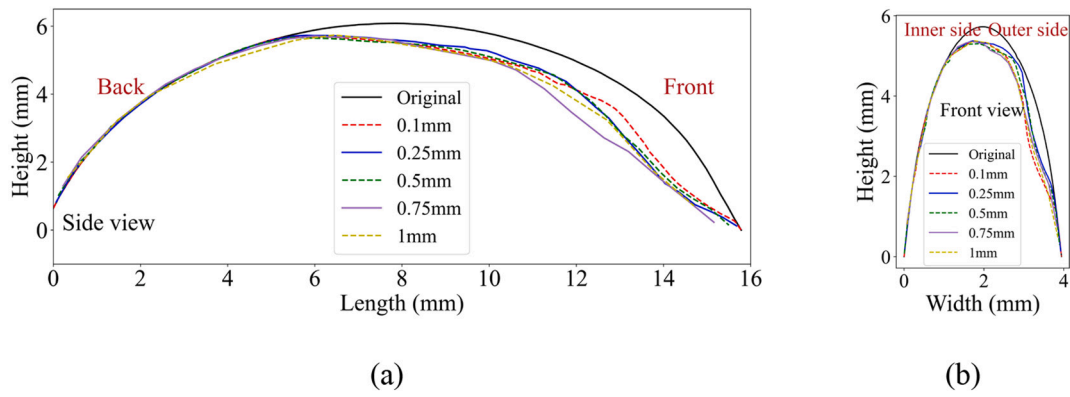


Fig. 11. Effect of mesh size on surface deformation (a) side view, (b) front view.

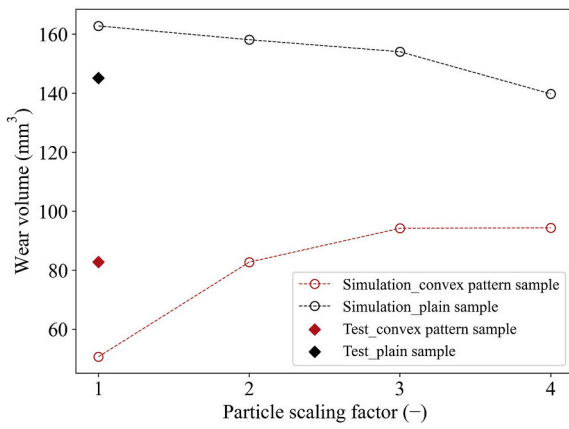


Fig. 12. Wear volume for benchmark test.

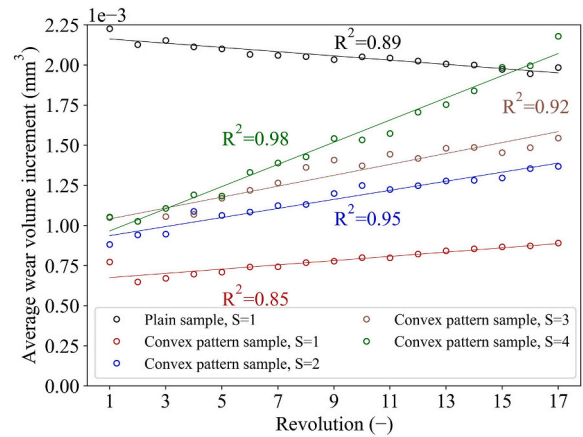


Fig. 14. Average wear volume increment for each revolution.

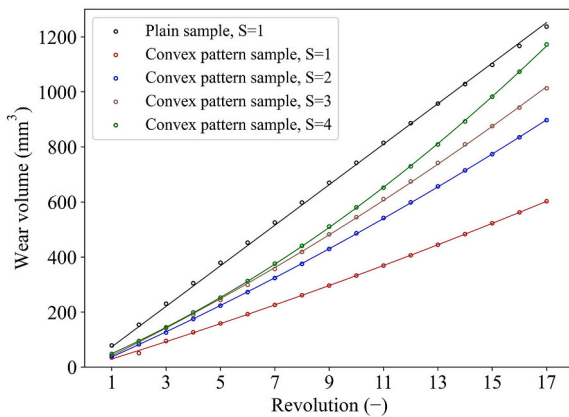


Fig. 13. Wear volume in relation to revolution (S indicates particle scaling factor).

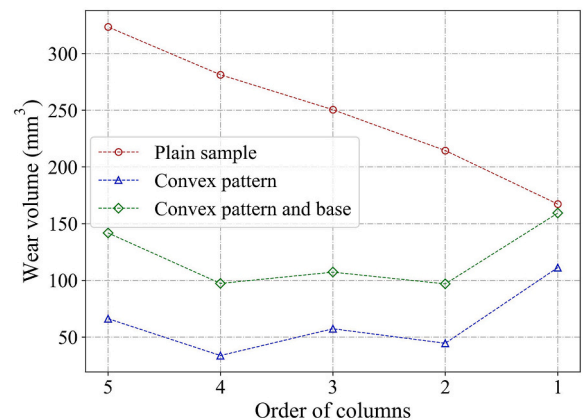


Fig. 15. Wear volume distribution of each column.

relatively small range from 75 ± 16 deg./s to 95 ± 34 deg./s. The convex pattern sample displays a decreasing trend as revolutions increase, from 198 ± 56 deg./s to 100 ± 26 deg./s. The angular velocity indicates that the plain sample has a minor effect on particle rolling behaviour, while the convex pattern sample facilitates rolling and therefore reduces sliding. As the convex pattern continues to deform, particles roll less readily due to sample deformation. Although angular velocity decreases for the convex pattern sample, it is still higher than for the plain sample.

Fig. 20 indicates the particle velocity at the bottom layer. Particle velocity shows an opposite trend to angular velocity. The particles in the

plain sample exhibit velocities exceeding 500 mm/s, while the convex pattern sample sees much lower velocities of <250 mm/s. As particle velocity is related to sliding distance, this means that particles slide less far in the convex pattern sample than in the plain sample, resulting in less wear. The particle flow behaviour is consistent with the previous studies. For a detailed explanation, please refer to [38].

To explicitly demonstrate particle flow behaviour, the relative particle angular and transitional velocity distributions at the 5th revolution are constructed as shown in Fig. 21 and Fig. 22. It should be noted that the relative velocity is based on the corresponding average value from the plain sample. For the angular velocity, Fig. 21 shows that the

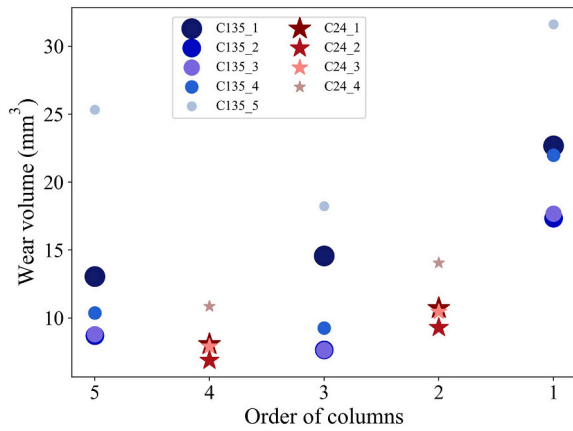


Fig. 16. Wear volume distribution of individual convex elements.

particles have a greater tendency to roll on the convex pattern sample (Fig. 21 (b)) than on the plain sample (Fig. 21 (a)). This indicates that the convex pattern sample facilitates the rolling of particles.

Fig. 22 illustrates relative particle transitional velocity. The arrows in the circles represent the directions of particle velocity. For the plain sample shown in Fig. 22 (a), the particles flow in a consistent pattern over the whole sample. The particles at the outside have higher velocities because of the rotating effect of the circle wear tester. For the convex pattern sample shown in Fig. 22 (b), the particles have a lower transitional velocity compared to that of the plain sample, leading to a shorter sliding distance. After contact with the convex pattern, the moving direction of the particles alters and weakens the direct contact with the convex pattern. In addition, the convex pattern has a guiding effect on particles and forces them to move among the convex elements.

5.3.2. Normal force

Normal force influences sliding wear as indicated in Eq. (1). Fig. 23 compares the normal force in the convex pattern and plain samples. The normal force has a similar tendency to the angular velocity shown in Fig. 21. For the plain sample, the normal force has a relatively narrow range from 15 ± 3 N to 18 ± 2 N with minor fluctuation, which means that the deformation of the plain sample has a minor effect on the contact between particles and the sample. For the convex pattern sample, the normal force displays a decreasing trend from 28 ± 7 N to 18 ± 4 N. This indicates that the deformation of the convex pattern weakens

the normal contact with particles and that deformation alters the contact between the sample and the particles.

Fig. 24 indicates the normal force distribution based on the division of the sample shown in Fig. 3. The plain sample exhibits an increasing trend due to particle accumulation, as explained in the previous study [12]. For the convex pattern sample, the normal force is higher than that of the plain sample over the five columns. Since the first column of the convex pattern sample initializes the bulk flow behaviour, it takes up the majority of the total force (>65%) of the column. Therefore, the first column of the convex pattern sample presents the highest wear volume and the most severe wear deformation.

6. Conclusions

This study investigates the deformation of a convex pattern sample caused by sliding wear with respect to different particle size distributions. The aim is to provide clarity on how effectively the deformed sample reduces sliding wear compared to a plain sample.

The wear experiments indicate that the convex pattern sample reduces wear by 43% compared to a plain sample and that there is a linear relation between wear volume loss and test time for both the plain and convex pattern samples. The sample deformation shows that the sides of the convex pattern sample are subjected to more severe wear.

The numerical model is validated by comparing the wear volume of a plain sample, which showed wear reduction rates of 68.9% and 43.0% for the simulation and experiments, respectively. As the 56-h experiment can be reliably represented by 2 revolutions of simulation, a scaling factor of 40,000 is obtained comparing effective distance travelled in the experiment and simulation.

The numerical results indicate a linear and quadratic relation between wear volume and the number of revolutions for the plain and convex pattern sample, correspondingly. This implies that the trend of wear reduction of the convex pattern surface weakens as a result of the deformation. Furthermore, particle size has a significant effect on the effectiveness of wear reduction of the convex pattern sample, with smaller particles corresponding to less wear.

The deformation distribution of the convex pattern depends on the contact behaviour of the particle flow, and the deformation accelerates as the rolling effect of the convex pattern weakens. For the deformation of the convex pattern, the convex elements at the sides of the sample experience severer deformation, similar to what was observed in the experiment.

The essential mechanism of the convex pattern sample on wear

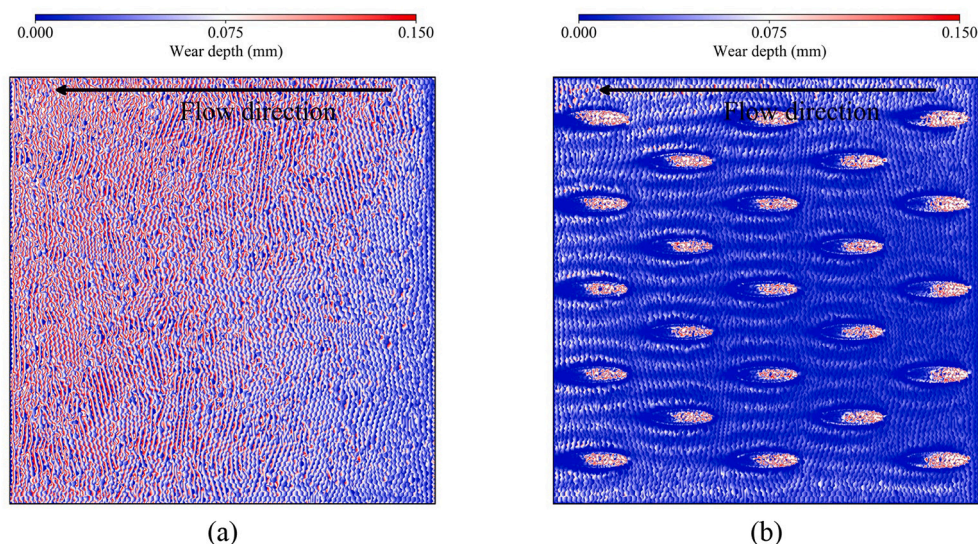


Fig. 17. Wear distribution (a) plain sample, (b) convex pattern sample.

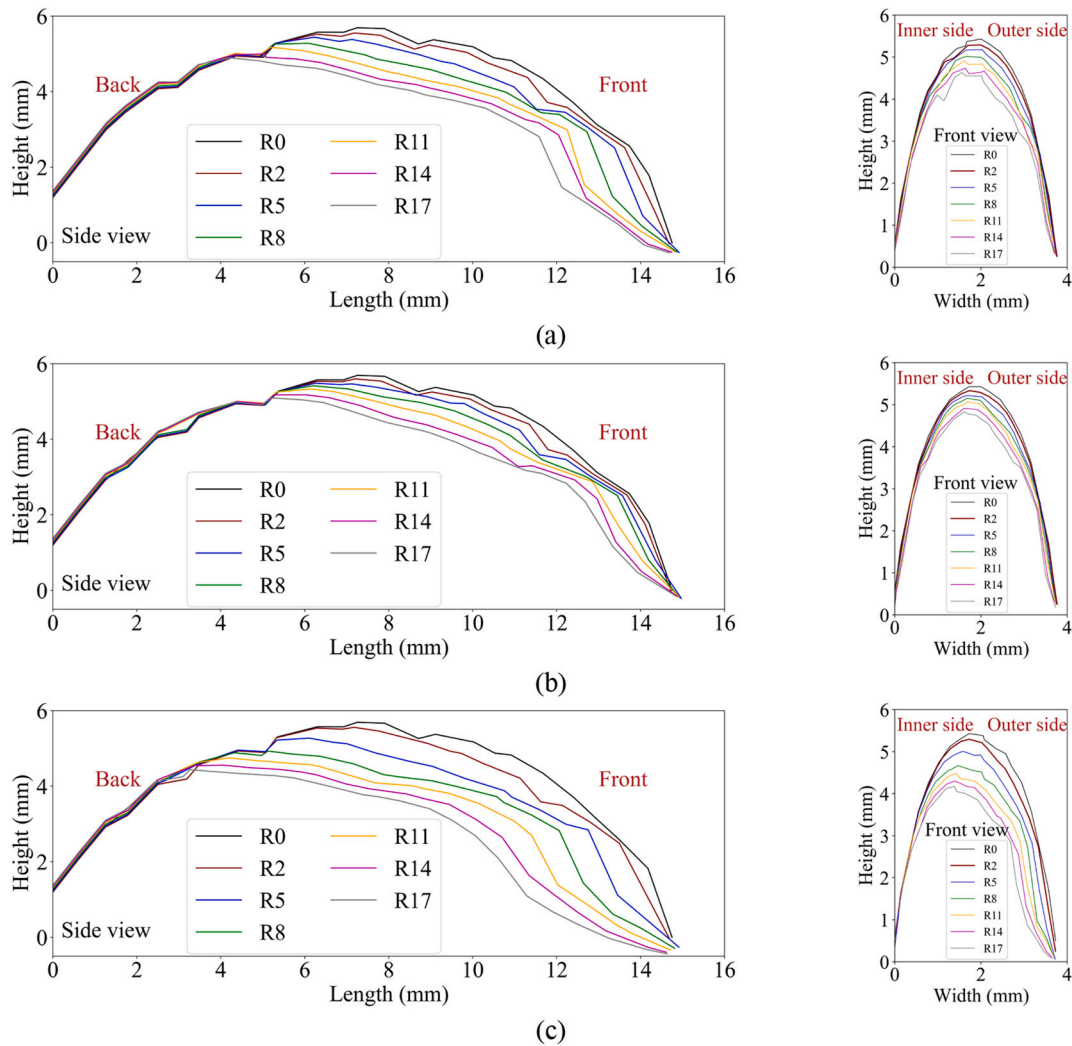


Fig. 18. Convex elements deformation from simulations (a) C11 (1st column 1st convex element), (b) C13 (1st column 3rd), (c) C15 (1st column 5th).

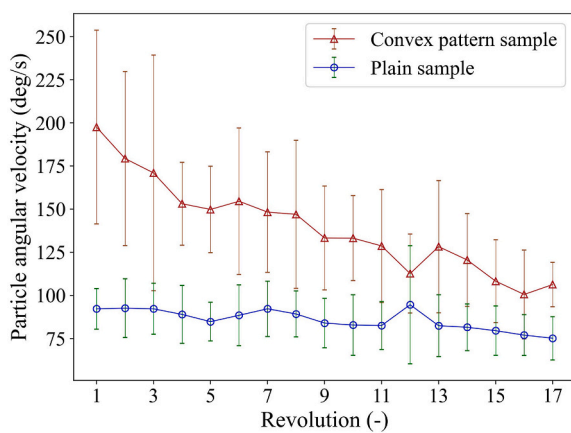


Fig. 19. Angular velocity of particles in relation to revolution (Error bar indicates standard deviation).

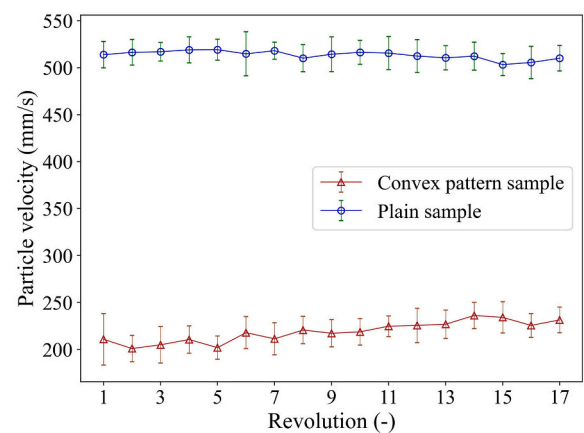


Fig. 20. Particle velocity in relation to revolution (Error bar indicates standard deviation).

reduction relies on altering the flow behaviour of particles. The contact behaviour of particles at the bottom layer indicates that the convex pattern decelerates the transitional velocity of particles and facilitates rolling, leading to a shorter sliding distance than a plain sample.

Future work will focus on two aspects. First, the mesh distortion issue

should be solved to fully wear out the convex pattern, so the entire deformation behaviour of the convex pattern can be evaluated. Second, the wear experiments should continue to generate sufficient wear to compare the wear behaviour of the sample with the numerical model. To accelerate the deformation of the convex pattern sample, a deeper

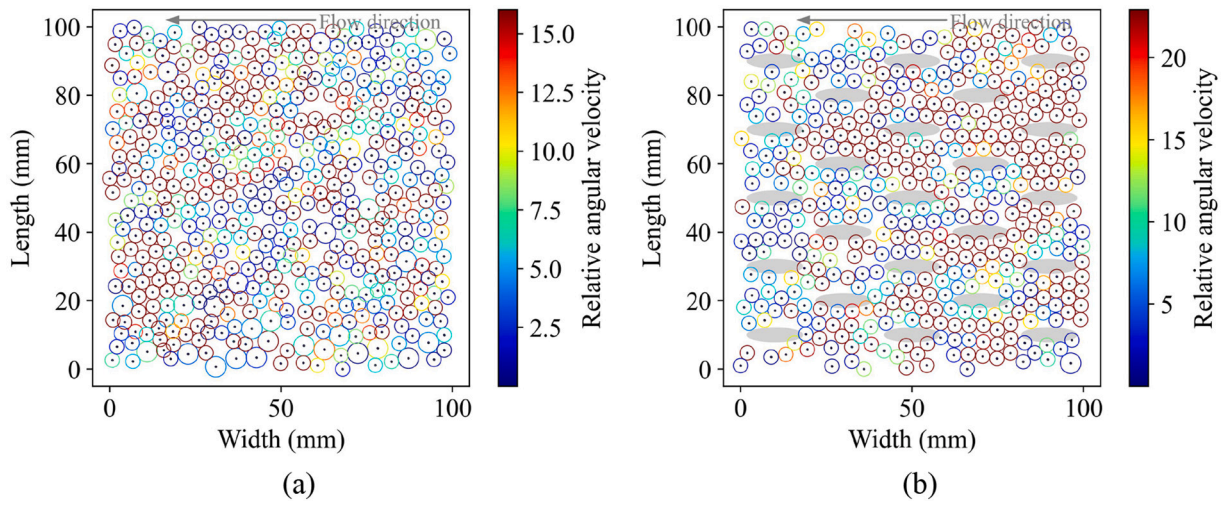


Fig. 21. Relative angular velocity distribution of particles in the (a) plain sample, (b) convex pattern sample (The circles and colors represent the particles and the relative angular velocities of particles, respectively).

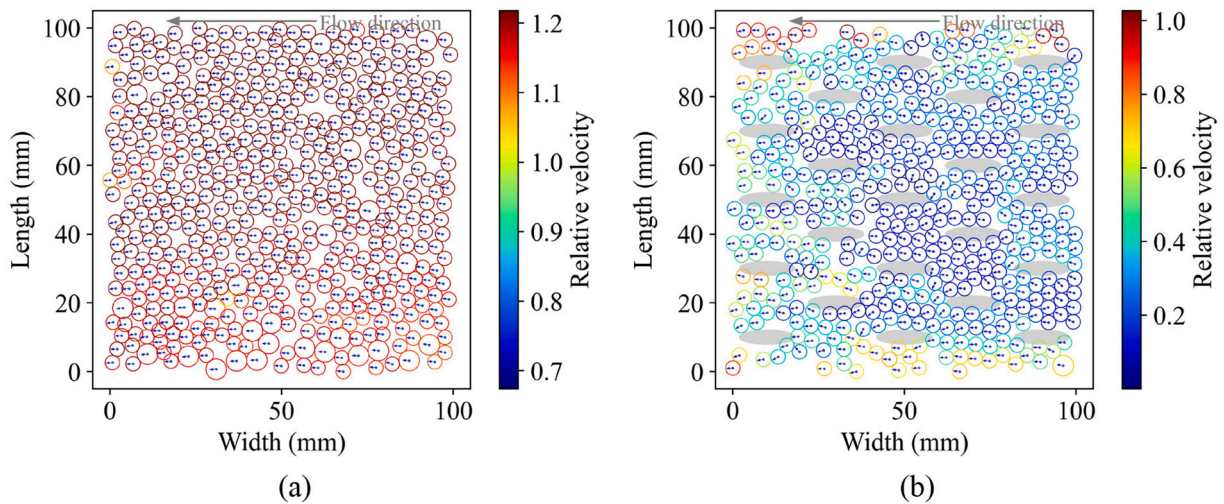


Fig. 22. Relative velocity distribution of particles in the (a) plain sample, (b) convex pattern sample (The circles, colors, and arrows represent the particles, the relative velocities of particles, and the direction of the particle velocities, respectively).

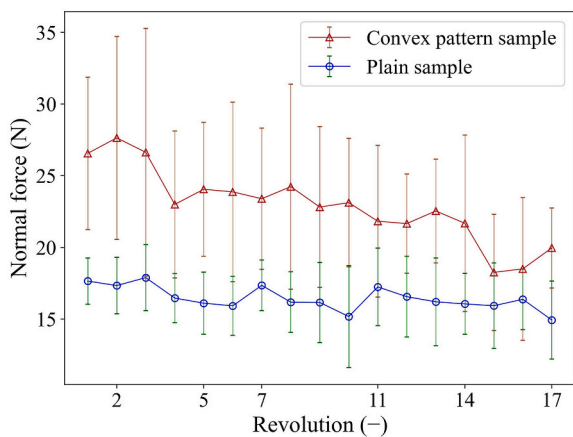


Fig. 23. Normal force in relation to revolution (Error bar indicates standard deviation.)

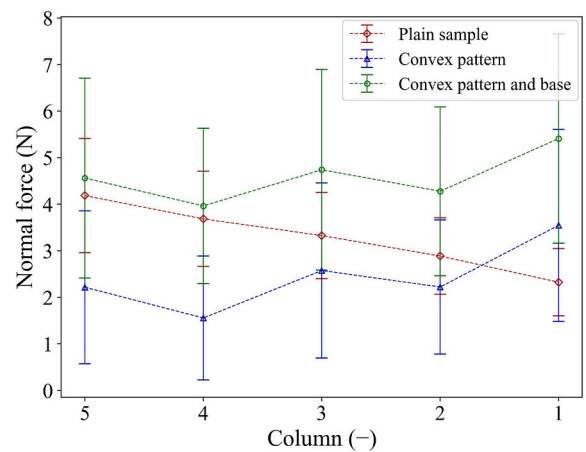


Fig. 24. Normal force distribution (Error bar indicates standard deviation).

particle bed will be used.

Formatting of funding resources

This work was supported by the China Scholarship Council [grant numbers CSC No. 201806170036].

Credit statement

Conceptualization, Yunpeng Yan; data curation, Yunpeng Yan; formal analysis, Yunpeng Yan; funding acquisition, Yunpeng Yan; investigation, Yunpeng Yan; methodology, Yunpeng Yan; project administration, Rudy Helmons, Dingena Schott, Michael Carr, and Craig Wheeler; resources, Yunpeng Yan; software, Yunpeng Yan; supervision,

Rudy Helmons and Dingena Schott; visualization, Yunpeng Yan; writing—original draft, Yunpeng Yan; Writing—review & editing, Yunpeng Yan, Rudy Helmons, Dingena Schott, Michael Carr, and Craig Wheeler. All authors have read and agreed to the published version of the manuscript.

Declaration of Competing Interest

This paper has no conflict of interest.

Data availability

The authors are unable or have chosen not to specify which data has been used.

Appendix A. Appendix

Fig. A.1 illustrates the sequence of mesh deformation.

- 1) The contact between the particle and the mesh elements is detected and the forces are calculated based on the contact model.
- 2) The loss of the material is evaluated based on the Archard wear model.
- 3) The new positions of the elements and velocity of the particle are recalculated.
- 4) The element is displaced in its normal direction.

Therefore, wear loss can be represented by deforming the triangular meshes subjected to abrasive wear.

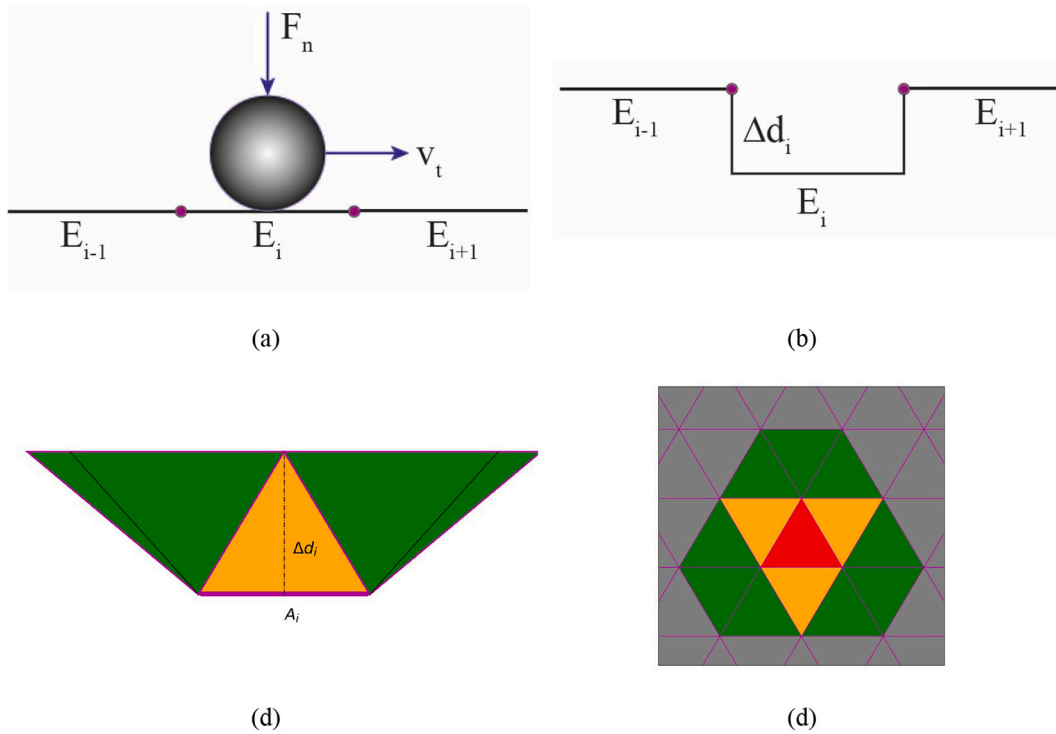


Fig. A.1. Mesh deformation procedure (a) particle in contact with the surface E_i of the mesh element, (b) displacement of the mesh element, (c) side view of the interconnection between nodes, and (d) top view of the wear representation.

The wear volume of the i^{th} element at each time step Δt is expressed by Eq. (A.1).

$$\Delta V_i = \int_t^{t+h} \alpha_s F_n \|v_t\| dt \approx \alpha_s F_n \|v_t\| \Delta t \tag{A.1}$$

The differential displacement (wear depth) Δd_i for the i^{th} element is related to the element area and the relations are denoted as Eqs. (A.2) and (A.3),

$$\Delta d_i = \frac{\Delta V_i}{A_i} \tag{A.2}$$

$$A_i = \frac{|(p_1 - p_2) \times (p_1 - p_3)|}{2} \tag{A.3}$$

where p_1, p_2, p_3 are the positions of a node of a triangular element.

The wear depth $d_i^{t+\Delta t}$ and the new position $p_k^{t+\Delta t}$ of nodes of the mesh element at time $t + \Delta t$ are obtained through Eqs. (A.4) and (A.5),

$$d_i^{t+\Delta t} = d_i^t + \Delta d_i^t \cdot \hat{n}_i \tag{A.4}$$

$$p_k^{t+\Delta t} = p_k^t + \Delta d_i^t \cdot \hat{n}_i (k = 1, 2, 3) \tag{A.5}$$

Equation where \hat{n}_i is the normal vector of the element. By interconnecting the common nodes of the element faces, it is possible to obtain continuity in the deformation of the surface, generating a smoothed wear pattern [29]. As the mesh element is in motion, the coordinates of the central point p_c , which represents the position of the i th element, is calculated before obtaining the accumulated wear V_i of the mesh element, as expressed by Eq. (A.6).

$$p_{ci} = \frac{p_{1,i} + p_{2,i} + p_{3,i}}{3} \tag{A.6}$$

Then, the wear volume of each element is integrated through Eq. (A.7).

$$V_i = V_i + \left| p_{c_j}^{t+h} - p_{c_j}^t \right| A_i \tag{A.7}$$

The total volume loss of the whole surface is obtained by adding the volume of each element together, as expressed by Eq. (A.8)

$$V = \sum_i^n V_i \tag{A.8}$$

Fig. A.2 demonstrates the procedure of wear contour reconstruction.

- 1) The sample is scanned to formulate a point cloud where the coordinates of each point are saved.
- 2) The orientation of the sample is confirmed based on a marker on the sample by importing the point cloud into Meshlab.
- 3) The point cloud of individual convex are extracted based on the location of the convex at the sample, and Python is used to process the data points from this step.
- 4) The data points of wear contour are extracted from the point cloud of individual convex.
- 5) The data points are visualized by rotating 2 degrees to consist with the inclination of the sample on the tester.

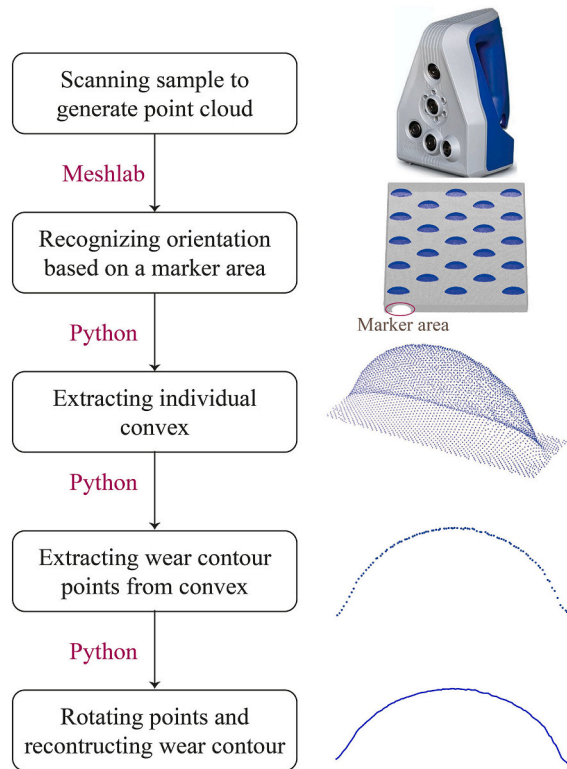


Fig. A.2. Procedure of wear contour reconstruction.

References

[1] D. Schulze, *Powders and Bulk Solids: Behavior, Characterization, Storage and Flow* 2008, 2003.

[2] A.W. Roberts, Chute performance and design for rapid flow conditions, *Chem. Eng. Technol.* 26 (2003) 163–170, <https://doi.org/10.1002/ceat.200390024>.

[3] I. Hutchings, P. Shipway, *Sliding Wear*, 2nd ed, Elsevier Ltd., 2017, <https://doi.org/10.1016/b978-0-08-100910-9.00005-2>.

[4] H.L. Costa, J. Schille, A. Rosenkranz, Tailored surface textures to increase friction—a review, *Friction*. 10 (2022) 1285–1304, <https://doi.org/10.1007/s40544-021-0589-y>.

- [5] M. Marian, A. Almqvist, A. Rosenkranz, M. Fillon, Numerical micro-texture optimization for lubricated contacts—a critical discussion, *Friction*. (2022), <https://doi.org/10.1007/s40544-022-0609-6>.
- [6] H. Yu, Z. Han, J. Zhang, S. Zhang, Bionic design of tools in cutting: reducing adhesion, abrasion or friction, *Wear*. 482–483 (2021), 203955, <https://doi.org/10.1016/j.wear.2021.203955>.
- [7] B. Chirende, J. Li, L. Wen, T.E. Simalenga, Effects of bionic non-smooth surface on reducing soil resistance to disc ploughing, *Sci. China Technol. Sci.* 53 (2010) 2960–2965, <https://doi.org/10.1007/s11431-010-4128-8>.
- [8] X.F. Yang, R. Xia, H.W. Zhou, L. Guo, L.J. Zhang, Bionic surface design of cemented carbide drill bit, *Sci. China Technol. Sci.* 59 (2016) 175–182, <https://doi.org/10.1007/s11431-015-5942-9>.
- [9] D. Gropper, L. Wang, T.J. Harvey, Hydrodynamic lubrication of textured surfaces: a review of modeling techniques and key findings, *Tribol. Int.* 94 (2016) 509–529, <https://doi.org/10.1016/j.triboint.2015.10.009>.
- [10] J.F.V. Vincent, O.A. Bogatyreva, N.R. Bogatyrev, A. Bowyer, A.K. Pahl, Biomimetics: its practice and theory, *J. R. Soc. Interface* 3 (2006) 471–482, <https://doi.org/10.1098/rsif.2006.0127>.
- [11] G. Chen, *Surface Wear Reduction of Bulk Solids Handling Equipment Using Bionic Design*, Delft University of Technology, 2017.
- [12] Y. Yan, R. Helmons, C. Wheeler, D. Schott, Optimization of a convex pattern surface for sliding wear reduction based on a definitive screening design and discrete element method, *Powder Technol.* 394 (2021) 1094–1110, <https://doi.org/10.1016/j.powtec.2021.09.041>.
- [13] P.A. Cundall, O.D.L. Strack, A discrete numerical model for granular assemblies, *Geotechnique*. 29 (1979) 47–65, <https://doi.org/10.1680/GEOT.1979.29.1.47>.
- [14] P.W. Cleary, Predicting charge motion, power draw, segregation and wear in ball mills using discrete element methods, *Miner. Eng.* 11 (1998) 1061–1080, [https://doi.org/10.1016/s0892-6875\(98\)00093-4](https://doi.org/10.1016/s0892-6875(98)00093-4).
- [15] P.W. Cleary, P. Owen, Development of models relating charge shape and power draw to SAG mill operating parameters and their use in devising mill operating strategies to account for liner wear, *Miner. Eng.* 117 (2018) 42–62, <https://doi.org/10.1016/j.mineng.2017.12.007>.
- [16] P.W. Cleary, M. Sinnott, R. Morrison, Analysis of stirred mill performance using DEM simulation: part 2 - coherent flow structures, liner stress and wear, mixing and transport, *Miner. Eng.* 19 (2006) 1551–1572, <https://doi.org/10.1016/j.mineng.2006.08.013>.
- [17] L. Xu, S. Bao, Y. Zhao, Multi-level DEM study on liner wear in tumbling mills for an engineering level approach, *Powder Technol.* 364 (2020) 332–342, <https://doi.org/10.1016/j.powtec.2020.02.004>.
- [18] L. Xu, K. Luo, Y. Zhao, J. Fan, K. Cen, Influence of particle shape on liner wear in tumbling mills: a DEM study, *Powder Technol.* 350 (2019) 26–35, <https://doi.org/10.1016/j.powtec.2019.03.033>.
- [19] L. Xu, K. Luo, Y. Zhao, Numerical prediction of wear in SAG mills based on DEM simulations, *Powder Technol.* 329 (2018) 353–363, <https://doi.org/10.1016/j.powtec.2018.02.004>.
- [20] E. Rojas, V. Vergara, R. Soto, Case study: discrete element modeling of wear in mining hoppers, *Wear*. 430–431 (2019) 120–125, <https://doi.org/10.1016/j.wear.2019.04.020>.
- [21] Á. Kalácska, P. De Baets, D. Fauconnier, F. Schramm, L. Frerichs, J. Sukumaran, Abrasive wear behaviour of 27MnB5 steel used in agricultural tines, *Wear*. 442–443 (2020), <https://doi.org/10.1016/j.wear.2019.203107>.
- [22] E. Katinas, R. Chotėborský, M. Linda, V. Jankauskas, Wear modelling of soil ripper tine in sand and sandy clay by discrete element method, *Biosyst. Eng.* 188 (2019) 305–319, <https://doi.org/10.1016/j.biosystemseng.2019.10.022>.
- [23] J.T. Kalala, M.H. Moys, Discrete element method modelling of liner wear in dry ball milling, *J. South. Afr. Inst. Min. Metall.* 104 (2004) 597–602.
- [24] P.M. Esteves, D.B. Mazzinghy, R. Galéry, L.C.R. Machado, Industrial vertical stirred mills screw liner wear profile compared to discrete element method simulations, *Minerals*. 11 (2021) 1–20, <https://doi.org/10.3390/min11040397>.
- [25] D. Boemer, J.P. Ponthot, A generic wear prediction procedure based on the discrete element method for ball mill liners in the cement industry, *Miner. Eng.* 109 (2017) 55–79, <https://doi.org/10.1016/j.mineng.2017.02.014>.
- [26] F. Schramm, V. Kalácska, J. Pfeiffer, P. De Sukumaran, L. Baets, Frerichs, modelling of abrasive material loss at soil tillage via scratch test with the discrete element method, *J. Terramechanics*. 91 (2020) 275–283, <https://doi.org/10.1016/j.jterra.2020.08.002>.
- [27] G. Chen, D.L. Schott, G. Lodewijks, Sensitivity Analysis of DEM Prediction for Sliding Wear by Single iron Ore Particle, *Eng. Comput. (Swansea, Wales)* vol. 34, 2017, pp. 2031–2053, <https://doi.org/10.1108/EC-07-2016-0265>.
- [28] Y. Yan, R. Helmons, D. Schott, Pin-on-disc modelling with mesh deformation using discrete element method, *Mater.* 15 (2022) 1813, 15 (2022) 1813, <https://doi.org/10.3390/MA15051813>.
- [29] F. Perazzo, R. Löhner, F. Labbe, F. Knop, P. Mascaró, Numerical modeling of the pattern and wear rate on a structural steel plate using DEM, *Miner. Eng.* 137 (2019) 290–302, <https://doi.org/10.1016/j.mineng.2019.04.012>.
- [30] J. Jäger, Elastic contact of equal spheres under oblique forces, *Arch. Appl. Mech.* 63 (1993) 402–412, <https://doi.org/10.1007/BF00805740>.
- [31] *D.E.M. Solutions, EDEM 2.3 User Guide, Edinburgh, Scotland, UK, 2010.*
- [32] J.F. Archard, Contact and rubbing of flat surfaces, *J. Appl. Phys.* 24 (1953) 981–988, <https://doi.org/10.1063/1.1721448>.
- [33] J. de Bono, H. Li, G. McDowell, A new abrasive wear model for railway ballast, *Soils Found.* 60 (2020) 714–721, <https://doi.org/10.1016/j.sandf.2020.05.001>.
- [34] L. Godino, I. Pombo, J. Girardot, J.A. Sanchez, I. Iordanoff, Modelling the wear evolution of a single alumina abrasive grain: analyzing the influence of crystalline structure, *J. Mater. Process. Technol.* 277 (2020), 116464, <https://doi.org/10.1016/j.jmatprotec.2019.116464>.
- [35] A. Ramalho, J.C. Miranda, The relationship between wear and dissipated energy in sliding systems, *Wear*. 260 (2006) 361–367, <https://doi.org/10.1016/j.wear.2005.02.121>.
- [36] D. Forsström, P. Jonsén, Calibration and validation of a large scale abrasive wear model by coupling DEM-FEM: local failure prediction from abrasive wear of tipper bodies during unloading of granular material, *Eng. Fail. Anal.* 66 (2016) 274–283, <https://doi.org/10.1016/j.engfailanal.2016.04.007>.
- [37] S.J. Wiche, S. Keys, A.W. Roberts, Abrasion wear tester for bulk solids handling applications, *Wear*. 258 (2005) 251–257, <https://doi.org/10.1016/j.wear.2004.09.014>.
- [38] Y. Yan, R. Helmons, D. Schott, The influence of particle size on the sliding wear of the con-vox pattern surface, *Minerals*. 12 (2) (2021), <https://doi.org/10.3390/min12020139>.